Pore Structures of Ordered Large Cage-Type Mesoporous Silica FDU-12s

Ting Yu,[†] **Hong Zhang,**[‡] **Xuewu Yan,**[†] **Zhengxia Chen,**[†] **Xiaodong Zou,**[§] **Peter Oleynikov,**[§] **and Dongyuan Zhao*,**[†]

Department of Chemistry, Shanghai Key Laboratory of Molecular Catalysis and Innovative Materials, Advanced Materials Laboratory, Fudan University, Shanghai, 200433, P. R. China, Key Lab of Molecular Engineering of Polymers and Engineering Center of Coating of Chinese Ministry of Education, Fudan University, Shanghai 200433, P. R. China, Materials Science and Engineering, Central South University, 410083, Changsha, P. R. China, and Structural Chemistry, Stockholm University, SE-106 91 Stockholm, Sweden

The pore variations of ordered cage-type mesoporous silica FDU-12s have been analyzed in detail by PXRD, SAXS, nitrogen sorption, and electron crystallography. FDU-12s with a cubic symmetry (space group, $Fm\bar{3}m$) were templated by amphiphilic triblock copolymer F127 with the addition of 1,3,5-trimethylbenzene and KCl under an acidic condition. Three typical samples with different unit cell sizes, pore cage diamters, and entrance sizes were obtained from different synthesis and hydrothermal treatment temperatures, as indicated by the differences in the PXRD and SAXS patterns. The pore structure changes in the three materials were observed by nitrogen adsorption/desorption and 3-D reconstruction of HRTEM images taken from different crystal orientations. The approximate pore structures of FDU-12s can be regarded as a face-centered cubic (fcc) close-packing of spherical cages, each connected to 12 nearest neigboring cages. However, the ideal spherical model is only valid for the FDU-12s prepared at a low temperature (L-FDU-12-100). The cage shape of the FDU-12s synthesized at a high temperature deviates from perfect spheres and is accompanied by an entrance enlargement. The temperature-dependent behavior of the PEO block is discussed with regard to its influence on the micelles and hence the cage configuration. The better understanding of the formation mechanism via the combined characterization techniques and modeling may lead to a more rational approach for tuning the pore cages and entrances of the mesoporous FDU-12 materials.

Introduction

In the past decades, porous materials have attracted great scientific and industrial interest due to their appealing structures and potential applications in separation, purification, catalysis, devices, and so forth.[1−3] The developing community of ordered mesoporous materials has carried on this exploration of the mesoscopical territory, which promises their unique capacities related to large molecules and their transportation in confined space.[4−9] Thus rational control and adjustment of pores have been continually focused during the synthesis of ordered mesoporous materials with diverse intrinsic properties.[10−15] Ordered cage-type mesoporous silica materials with large and well-controlled pore cages and entrances such as SBA-6, SBA-16, FDU-1, KIT-5, and FDU-12 are of great interest.[16−25] The supercages with multidirectional pore openings of these materials are believed to be advantageous over the channel-like mesopore systems.[24] For instance in SBA-16 materials, each pore cage is connected to the eight nearest neighboring cages as suggested by the electron crystallography study.[16] The relatively small entrance size of these cages hinders diffusion of macromolecules into large cages thus limiting the applications in encapsulation of biomolecules. However, the entrance sizes could be enlarged by increasing hydrothermal temperatures and time.[21,22,24,26,27] Recently, mesoporous silica FDU-12 materials with various unit cell sizes have been synthesized with the aid

of salts and a swelling agent. The cage and entrance size could be controlled by tailoring the amount of swelling agent, synthesis, and hydrothermal treatment temperature.[22,25] It is noted that the structure changes of FDU-12 materials are reflected in the variation of their diffraction patterns.

Some problems for structural analysis of mesoporous materials by powder X-ray diffraction (PXRD) are the lack of enough diffraction peaks, overlapping of the peaks, and loss of structure factor phase information. For cage-type mesoporous materials with a face-centered-cubic (fcc) close-packing, stacking faults often occur along the body diagonal of the cubic cell. The loss of structure ordering caused by the stacking faults led to difficulties in structural analysis of these materials, such as for SBA-12, FDU-1, and SBA-2.[21,28,30] The successful preparation of a pure 3-D cage-type mesoporous silica KIT-5 with $Fm\bar{3}m$ symmetry by Freddy et al. promoted its structural characterization by PXRD, N_2 sorption, and transmission electron microscopy (TEM) analysis.[23] We have also successfully synthesized highly ordered large cage-type $Fm\bar{3}m$ mesoporous silica FDU-12s with high purity and consisting of uniform domains.[22,25] However, the pore structures were only characterized qualitatively by PXRD and TEM analysis.

In this work, a detailed TEM and nitrogen sorption analysis of the mesoporous FDU-12 materials is performed to understand the process of pore cage expansion and entrance enlargement. On the basis of the spherical/cylindrical model, the nonlocal density functional theory (NLDFT) analysis of the isotherms is applied to obtain general structural features of the mesoporous silica FDU-12s. 3-D structure models of the mesoporous silica FDU-12s were reconstructed from high-resolution TEM (HR-

* Address correspondence to this author. E-mail: dyzhao@fudan.edu.cn. Phone: 86-21-6564-2036. Fax: 86-21-6564-1740.
† Fudan University.
‡ Central South University.
§ Stockholm University.

TEM) images by electron crystallography, which is proved to be powerful in the structural elucidation of mesoporous silica materials.[16,29−34] Finally, pore morphologies of the different FDU-12s are compared with each other. The temperature-dependent behaviors of the PEO block and its role to the pore morphologies are discussed.[7,24,25,37−39]

Experimental Section

Chemicals. All chemicals were used as received without further purifications. Triblock copolymer poly(ethylene oxide)-*b*-poly(propylene oxide)-*b*-poly(ethylene oxide) Pluronic F127 ($EO_{106}PO_{70}EO_{106}$, MW = 12 600) were purchased from Aldrich. Tetraethyl orthosilicate (TEOS) (99%), 1,3,5-trimethylbenzene (TMB), and potassium chloride (KCl) were purchased from Shanghai Chemical Reagent Company. Millipore water was used in all experiments.

Synthesis. Ordered large cage-type mesoporous silica materials (FDU-12s) were prepared by using a low-temperature synthesis strategy (synthesis temperatures: 15 and 35 °C) with a high-temperature hydrothermal treatment (100 and 120 °C). This synthesis recipe was analogous to the sol−gel composition reported by Fan et al.[22,25]

L-FDU-12-100. A typical synthesis procedure was as follows: 1.0 g of F127 and 2.5 g of KCl were dissolved in 60 mL of 2 M HCl, then 2.2 g of TMB was added and the mixture was stirred at 15 °C for 24 h in a capped container. Next 4.1 g of TEOS was added to the resulting reaction mixture, which was left to stir for another 24 h at 15 °C before being transferred to an autoclave and kept at 100 °C for 72 h. The solid product was collected by filtration and dried at ambient condition (20 °C). The resulting powder was calcined at 550 °C in air for 5 h to obtain surfactant-free mesoporous silica L-FDU-12-100.

In the following, a scaled-up recipe was used to systematically investigate the effects of synthesis and hydrothermal treatment temperatures and reduce other factors. Materials from the same batch were hydrothermally treated at different temperatures, 100 (R-FDU-12-100) and 120 °C (R-FDU-12-120), respectively.

R-FDU-12-100. A typical synthesis procedure was as follows: 10.0 g of F127 and 25.0 g of KCl were dissovled in 600 mL of 2 M HCl and then 22.0 g of TMB was added and the mixture was stirred at 35 °C for 24 h in an capped container. Next 41.0 g of TEOS was added to the above solution with stirring at 35 °C for another 24 h before being transferred to an autoclave and kept at 100 °C for 24 h. The solid product was collected by filtration and dried at ambient condition (20 °C). Then 0.2 g of the as-made powder (denoted as **S1**) was mixed with 20 mL of 2 M HCl and the mixture was stirred for 30 min. The obtained slurry mixture was transferred into an autoclave and heated at 100 °C for 72 h. The solid product was collected by filtration and dried at ambient condition. The resulting powder was calcined at 550 °C in air for 5 h to obtain mesoporous silica R-FDU-12-100.

R-FDU-12-120. A typical synthesis procedure was as follows: 0.2 g of as-made powder (**S1**) from the same pot as R-FDU-12-100 was mixed with 20 mL of 2 M HCl and stirred for 30 min. The obtained slurry mixture was transferred into an autoclave and heated at 120 °C for 72 h. The solid product was collected by filtration and dried at ambient condition. The resulted powder was calcined at 550 °C in air for 5 h to obtain mesoporous silica R-FDU-12-120.

Characterization. The structure and pore changes of FDU-12 samples were determined by a combination of PXRD, small-angle X-ray scattering (SAXS), nitrogen adsorption/desorption, and TEM. The low-angle PXRD patterns were collected on a Bruker D4 Endeavor X-ray diffractometer with Ni-filtered Cu Kα radiation (λ = 0.15418 nm, 40 kV, 40 mA). SAXS profiles were obtained from Bruker NanoSTAR with a 2-D detector (HiSTAR) and X-ray beam pinhole collimated (40 kV, 30 mA). TEM were carried out on a JEOL-2011 transmission electron microscope (Cs = 1.0 mm, point resolution 0.23 nm) or FEI Tecnai G^2 20 S-TWIN transmission electron microscope (Cs = 1.2 mm, point resolution 0.24 nm), both operated at 200 kV. HRTEM images were recorded with a CCD-camera (model 794, Gatan, size 1024 × 1024, pixel size 25 × 25 μm) at 29 000−60 000 times magnification. Nitrogen adsorption/desorption isotherms were measured at −196 °C by using a Micromeritics ASAP Tristar 3000 volumetric adsorption system. The samples were degassed at 180 °C overnight on a vacuum line. The Brumauer−Emmett−Teller (BET) method was utilized to calculate the specific surface areas. The pore size distributions and cage entrance size of the calcined samples were derived from either adsorption or desorption branches of the isotherms based on the NLDFT sphere and cylinderical models, respectively.

Image Processing. HRTEM images taken along the [110] and [211] zone axes were chosen for further 3-D reconstruction since all the strongest reflections were presented at these two zone axes. The crystallographic image processing was based on the strategy of the MRC system and carried out with the software CRISP[40] and eMap.[41] It included the following steps: Fourier transform, CTF correction, lattice refinement, amplitude and phase extraction, origin refinement and symmetry determination, common origin searching, scaling of reflections from different projections by common reflections, and 3-D reconstruction of the electrostatic potential map.[42] For each HRTEM image, a thin and well-ordered area of the image was chosen so that the weak phase object approximation was fulfilled. A Fourier transform (512 × 512 pixels) was carried out from the thin area from which the *hkl* extinction rules and hence the space group could be determined. The contrast transfer function (CTF) was determined from the Fourier transform of the image and compensated for the image. Amplitude and phase were extracted from each diffraction spot on the Fourier transform. The 2-D plane symmetry was first determined from the extracted phases (*cmm* for [110] and *pmm* for [211] zone axes for all three samples) and then imposed on the amplitudes and phases. The symmetry imposed amplitudes and phases were regarded as the structure factor amplitudes and phases. Common reflections from different zone axes were used to scale the amplitudes and derive the origin position. From the structure factors derived through the combination of different data sets from the two zone axes, a 3-D electrostatic potential map of the unit cell was obtained from inverse Fourier transformatiom of the observed structure factors imposed with the space group symmetry.[42]

Results and Discussion

PXRD and SAXS Characterization. At a fixed TEOS−F127−TMB−KCl−HCl−H_2O molar ratio (1:0.004:1:1.68:6:157) of the starting mixtures, three FDU-12 samples were prepared with different synthesis temperature and hydrothermal treatment temperature. PXRD and SAXS patterns (Figure 1) show that the diffraction peaks of samples prepared at the low synthesis temperature (15 °C) or high hydrothermal treatment temperature (120 °C) were shifted to the low angle region, similar to the previous reports.[21,22,25] Though diffraction peaks of the FDU-12 samples are possibly overlapped, an attempt was still made to deduce the possible choices of the symmetry for all three samples.
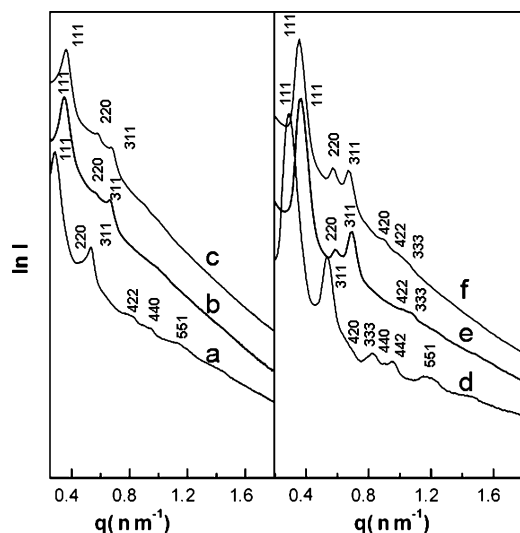
Ordered Large Cage-Type Mesoporous Silica FDU-12s

J. Phys. Chem. B, Vol. 110, No. 43, 2006 **21469**

Figure 1. PXRD patterns (left) and SAXS profiles (right) of calcined mesoporous silica FDU-12 samples: (a, d) L-FDU-12-100, (b, e), R-FDU-12-100, and (c, f) R-FDU-120. PXRD patterns are plotted as ln *I* to *q* to compare with SAXS profiles ($q = (4\pi \sin(\theta)/\lambda)$).
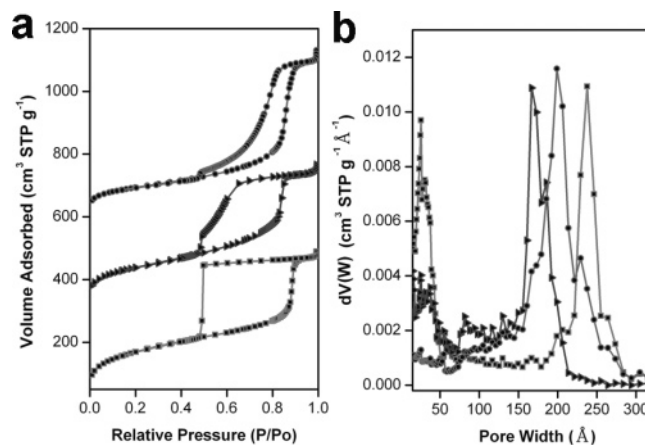

Figure 2. Nitrogen sorption isotherms (a) and pore size distribution (b) of calcined mesoporous silica FDU-12 samples. The plotted lines of L-FDU-12-100, R-FDU-12-100, and R-FDU-12-120 are denoted as solid squares, triangles, and circles, respectively. The scale of adsorption volume in panel a is shifted by 300 cm^3/g for R-FDU-12-100 and 600 cm^3/g for R-FDU-12-120.

The PXRD pattern of L-FDU-12-100 (Figure 1a) shows six resolved diffraction peaks with *d*-spacing ratios of $\sqrt{3}$:$\sqrt{8}$:$\sqrt{11}$: $\sqrt{24}$:$\sqrt{32}$:$\sqrt{51}$. The diffraction peaks can be indexed as the 111, 220, 311, 422, 440, and 551 reflections in a cubic unit cell of 39.0 nm. The SAXS profile of L-FDU-12-100 (Figure 1d) reveals eight resolved diffraction peaks with *q* values of 0.277, 0.530, 0.701, 0.821, 0.903, 0.967, 1.155 nm^{-1}, respectively. These diffraction peaks can be indexed as the 111, 311, 420, 333 (or 511), 440, 442, and 551 reflections in a cubic unit cell of 39.3 nm. The 200 diffraction peak is detected from a second derivative plot of the PXRD pattern. On the basis of these observations, the reflection conditions are summarized as follows: {*hkl*: $h + k, h + l, k + l = 2n$}, {*0kl*: $k, l = 2n$}, {*hhl*: $h + l = 2n$}, and {*h00*: $h = 2n$}. The highest space group $Fm\bar{3}m$ is chosen among the possible space groups: $F23$, $Fm\bar{3}$, $F432$, $F\bar{4}3m$, and $Fm\bar{3}m$.

The PXRD pattern of R-FDU-12-100 (Figure 1b) shows three diffraction peaks with *d*-spacing ratios of $\sqrt{3}$:$\sqrt{8}$:$\sqrt{11}$. Five diffraction peaks are clearly observed from its SAXS pattern (Figure 1e) with *q*-values of 0.356, 0.583, 0.701, 1.024, 1.081 nm^{-1}, which can be indexed as the 111, 220, 311, 422, 333 (or 511) reflections in a cubic unit cell of 30.5 nm. The reflection conditions are {*hkl*: $h + k, h + l, k + l = 2n$}, {*0kl*: $k, l = 2n$}, and {*hhl*: $h + l = 2n$}. Although the 200 diffraction peak could not be detected here, its presence could be confirmed by the Fourier transform of HRTEM as will be discussed below. Therefore, the space group of R-FDU-12-100 agrees with the conditions required for $Fm\bar{3}m$.

The PXRD pattern of R-FDU-12-120 (Figure 1c) shows three resolved diffraction peaks with *d*-spacing ratios of $\sqrt{3}$:$\sqrt{8}$:$\sqrt{11}$. The SAXS pattern (Figure 1f) has a better resolution than that of R-FDU-12-100 and shows six diffraction peaks at *q* values of 0.356, 0.569, 0.683, 0.910, 0.981, and 1.067 nm^{-1}, respectively. These diffraction peaks can be assigned to 111, 220, 311, 420, 422, 333 reflections in a cubic unit cell of 31.2 nm, slightly larger than that of R-FDU-12-100 (30.5 nm) and much smaller than that of L-FDU-12-100. The reflection conditions are {*hkl*: $h + k = 2n, h + l, k + l = 2n$}, {*0kl*: $k, l = 2n$}, {*hhl*: $h + l = 2n$}. Similar to that of R-FDU-12-100, the space group of R-FDU-12-120 can be assigned as $Fm\bar{3}m$.

Besides the difference of *d*-spacing values, the relative diffraction intensities in the PXRD patterns vary with the synthesis and hydrothermal treatment temperature. To minimize the influences of preferred orientations, SAXS measurements were performed on ground powders by filling the sampling holes without a strong backpressure as commonly applied for PXRD measurements. In both cases, the same trend in relative intensity changes was observed, implying the existence of different internal pore structures in the three FDU-12 samples. Sakamoto et al. have first presented the 3-D mesostructure of SBA-12 based on the electrostatic potential maps obtained by electron crystallography.[30] The 3-D pore structure of SBA-12 could be described based on a simple cubic-close-packing (ccp) of spherical pores and it can be used as an approximate pore model of cage-type $Fm\bar{3}m$ mesoporous silica and also for understanding the adsorption/desorption behaviors of mesoporous materials. However, the simple spherical pore model is not sufficient for interpreting the pore structure variations indicated by the intensity changes in diffraction patterns of the different samples. The significant intensity differences of the 220 reflection, which is perpendicular to the direction of the entrance channels, may be correlated to the cage entrance enlargement. Modified sphere or cylinder models with several variables have been previously applied to refine the model upon the experimental PXRD patterns.[43-45] However, very little was done on the entrance enlargement based on the structure models obtained experimentally, for example, by nitrogen sorption and/or TEM.

N₂ Sorption. Nitrogen adsorption/desorption isotherms of the three FDU-12 samples prepared with different synthesis/ hydrothermal treatment temperatures are analogous to those large cage-type mesoporous materials such as SBA-16, FDU-1, KIT-5, etc.[8,21,23] The initial step of adsorption isotherms, representing the adsorption in micropores and formation of nitrogen multilayers on the pore walls, decreases with the rising synthesis and hydrothermal treatment temperatures. This phenomenon is typical for mesoporous materials templated by PEO−PPO−PEO triblock copolymers under hydrothermal treatment.[21,38] The NLDFT sphere model was applied in the calculation of the cage diameters due to their typical IV isotherm curves with an hysteresis loop.[35,36] As shown in Figure 2, after the hydrothermal treatment, the steepness of the adsorption branch together with the pore size distribution tends to be broader, indicating that the hydrothermal treatment causes the nonuniform cage expansion.

The detailed textural properties of three FDU-12 samples are listed in Table 1. The ratio of the mean pore size to the unit

TABLE 1: Textural and Structural Properties of Calcined Mesoporous Silica FDU-12s

sample	unit cell a (nm)^a	S_{BET} (m²/g)	pore vol (cm³/g)^b	pore size (nm)^c	entrance size (nm)^e	pore size vs unit cell^f	entrance size vs unit cell^f
L-FDU-12-100	39.3	610	0.73	23.7	<5	0.60	
R-FDU-12-100	30.5	496	0.69	16.7	6.3 (<5)^d	0.55	0.21
R-FDU-12-120	31.2	337	0.77	19.9	11.6 (<5)^d	0.64	0.37

^{a} Calculated from the SAXS profiles. ^{b} The total pore volumes were estimated from the amount adsorbed at the relative pressure of 0.98. ^{c} Calculated from the adsorption branch of the isotherms based on the NLDFT sphere model. ^{d} Calculated from desorption branch of the isotherms based on the NLDFT cylinder model. ^{e} Bimodal entrance size.[47] ^{f} Mean pore size and entrance size from the pore size distribution is divided by the unit cell parameter a in order to be compared with each other.

cell was calculated to be 0.60 for L-FDU-12-100, 0.55 for R-FDU-12-100, and 0.64 for R-FDU-12-120. The low synthesis temperature (15 °C) increased the relative pore size by 9% from 0.55 for R-FDU-12-100 to 0.60 for L-FDU-12-100, and the high hydrothermal treatment temperature (120 °C) induced a relatively pore size expansion by 16% from 0.55 for R-FDU-12-100 to 0.64 for R-FDU-12-120.

The ratio of the entrance size to the unit cell calculated based on the cylinder model was 0.21 for R-FDU-12-100 and 0.37 for R-FDU-12-120. The low synthesis temperature (15 °C) decreased the relative entrance from R-FDU-12-100 to L-FDU-12-100, although the relative pore size was increased by 9%. The high hydrothermal treatment temperature (120 °C) caused a large increase of the relative entrance size by 76% from 0.21 for R-FDU-12-100 to 0.37 for R-FDU-12-120, significantly larger than the corresponding increase of the relative pore size (16%). These entrance enlargement phenomena cannot be interpreted from the simple spherical model based on radial expansions of the spheres. The NLDFT method provided a preliminary and rough scheme about the pore structure variation of the FDU-12 materials. However, the sphere-cylinder model is composed of two separated parts (sphere + cylinder), and does not represent completely the real pore structures. It is necessary to obtain the 3-D pore structures by direct observations of the mesoporous FDU-12 materials, for example, by TEM.

HRTEM Image Processing. Typical HRTEM images of L-FDU-12-100 taken along the [110] and [211] directions and the corresponding Fourier diffractograms are shown in Figure 3, panels a and b. The space group was determined from the HRTEM images by analyzing both the amplitudes and the phases extracted from the HRTEM images. First the diffraction spots in Fourier diffractograms were indexed 111, 200, 220, 311, 222, 400, 331, 422, 333, 511, 440, 531, 442, and 600, respectively, by a face-centered cubic with a unit cell $a = 38.6$ nm (Table 2). The 200 reflection was among the strongest in the Fourier diffractogram, so the possible space groups are $F23$, $Fm\bar{3}$, $F432$, $F\bar{4}3m$, and $Fm\bar{3}m$. The symmetry of the [110] projection is cmm, as determined from the phases extracted from the HRTEM image. This can rule out the space groups $F23$ and $F\bar{4}3m$ that give the cm symmetry in the projection. The symmetry of the [211] projection is pmm and this rules out the space group $F\bar{4}3m$ (pm in the projection). Two space groups, $Fm\bar{3}$ and $Fm\bar{3}m$, are left, which can be distinguished from the [111] projection. The highest space group of $Fm\bar{3}m$ is finally assigned. The relatively small phase domains observed in the HRTEM images result in the broadening and overlapping of the diffraction peaks in the PXRD and SAXS patterns according to the Scherrer formula. Space group determination from HRTEM is more powerful than that from PXRD or SAXS since the former contains the structure factor phase information and has no overlapping problems.

The amplitudes and phases of the structure factors obtained from the HRTEM images taken along the [110] and [211] zone axes by crystallographic image processing are presented in Table
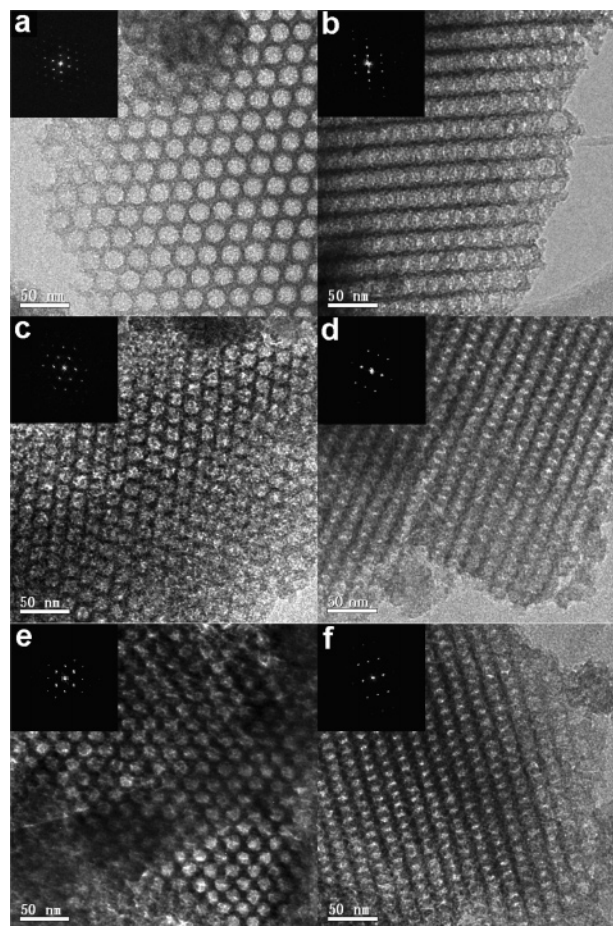

Figure 3. Typical HRTEM images and corresponding FT diffractograms of the calcined mesoporous silica FDU-12s: taken along the (a) [110] and (b) [211] directions of L-FDU-12-100, (c) [110] and (d) [211] directions of R-FDU-12-100, and (e) [110] and (f) [211] directions of R-FDU-12-120.

2, with all the amplitudes scaled relative to the 111 reflection, $F_{111} = 100.0$. It should be noted that all HRTEM images were taken at underfocus values so that the structure factor phases in Table 2 were shifted by π compared to those extracted from the HRTEM images (as given by Sakomoto et al.[30]). The two strongest and dominant reflections 111 and 200 have the structure factor phases π, which agree with the spherical pore model of a ccp lattice where the structure factor phases for all reflections are π. However, the structure factor phases for reflections 220, 311, 222, 400, and 331 in L-FDU-12-100 are zero, different from those of the spherical pore model and also those of SBA-12.[30] This suggests that the surface curvature of L-FDU-12-100 is different with the spherical pore model and previously resolved 3-D electrostatic potential map of SBA-12 prepared by using nonionic oligomer surfactant $C_{18}H_{37}EO_{10}$ as

Ordered Large Cage-Type Mesoporous Silica FDU-12s

J. Phys. Chem. B, Vol. 110, No. 43, 2006 **21471**

TABLE 2: Observed Structure Factor Amplitudes (F_{hkl}) and Phases (α_{hkl}) of Mesoporous Silica FDU-12s after the Corrections of CTF

$(h^2 + k^2 + l^2)$	L-FDU-12−100 ($a = 38.6$ nm)					R−FDU-12−100 ($a = 29.2$ nm)					R−FDU-12−120 ($a = 29.7$ nm)				
	h	k	l	F_{hkl}/F_{111}	α_{hkl}	h	k	l	F_{hkl}/F_{111}	α_{hkl}	h	k	l	F_{hkl}/F_{111}	α_{hkl}
3	1	1	1	−100.0	π	1	1	1	−100.0	π	1	1	1	−100.0	π
4	2	0	0	−58.6	π	2	0	0	−46.0	π	2	0	0	−43.2	π
8	2	2	0	4.5	0	2	2	0	8.6	0	2	2	0	13.0	0
11	3	1	1	7.1	0	3	1	1	11.9	0	3	1	1	7.6	0
12	2	2	2	8.1	0	2	2	2	6.9	0	2	2	2	3.7	0
16	4	0	0	4.2	0	4	0	0	3.9	0					
19	3	3	1	1.6	0	3	3	1	1.4	0	3	3	1	1.5	0
20						4	2	0	0.6	0	4	2	0	0.6	0
24	4	2	2	−1.0	π						4	2	2	−0.6	π
27	3	3	3	−1.1	π	3	3	3	−0.9	π					
27	5	1	1	−1.4	π	5	1	1	−1.4	π					
32	4	4	0	−0.9	π	4	4	0	−1.0	π	4	4	0	−1.1	π
35	5	3	1	−0.6	π	5	3	1	−0.5	π	5	3	1	−0.7	π
36	4	4	2	−0.9	π	4	4	2	−0.5	π					
36	6	0	0	−0.7	π	6	0	0	−1.0	π					

a template.[8,30] It should be noted that the 220 reflection is rather weak but still can be resolved by HRTEM.

HRTEM images and the corresponding Fourier diffractograms of R-FDU-12-100 taken from [110] and [211] directions are analogous to those of L-FDU-12-100 (Figure 3c,d). The reflections in the Fourier diffractograms can be indexed as 111, 200, 220, 311, 222, 400, 331, 420, 333, 511, 440, 531, 442, and 600, respectively, by a face-centered cubic with a unit cell $a = 29.2$ nm (Table 2). In a similar way as L-FDU-12-100, the space group of R-FDU-12-100 was assigned to be $Fm\bar{3}m$. The structure factors of R-FDU-12-100 are listed in Table 2. Similar to those of L-FDU-12-100, the structure factor phases of 111 and 200 are π and those of 220, 311, 222, 400, 331, and 420 are zero.

Panels e and f of Figure 3 show HRTEM images of R-FDU-12-120 taken along the [110] and [211] directions of a cubic phase with a unit cell $a = 29.7$ nm. The diffraction spots in the Fourier diffractogram can be indexed as 111, 200, 220, 311, 222, 331, 420, 422, 440, and 531, respectively, and the space group is also $Fm\bar{3}m$. Similar to those of L-FDU-12-100 and R-FDU-12-120, the structure factor phases of 111 and 200 are π and those of 220, 311, 222, 331, and 420 are zero.

The overall pore structures of FDU-12s are visualized from the 3-D electrostatic potential maps (Figure 4) reconstructed from structure factor amplitudes and phases in Table 2 by inverse Fourier transformation:[41]

$$\varphi(xyz) = V^{-1} \sum_h \sum_k \sum_l F(hkl) \exp[i\alpha(hkl)] \exp[-2\pi i(hx + ky + lz)]$$

where $\varphi(xyz)$, V, $F(hkl)$, and $\alpha(hkl)$ represent the electrostatic potential, cell volume, the observed structure factor amplitude and phase, respectively. Electrostatic potential maps are scaled to have the same unit cell size in order to be compared conveniently with each other (Figure 4). Herein the isoelectrostatic potential contours are expressed in isochromatic zones, where cold hue represents high electrostatic potential (Figure 4a−c). Circular isochromatic zones appear in the center of electrostatic potential maps (at $z = 0$ plane), which correspond to the pending interface between pores and silica walls. The pore surface of L-FDU-12-100 is more smoothed than that figured in the unit cell, since its unit cell is larger than that of the other two samples (R-FDU-12-100, R-FDU-12-120) by about 30% (Table 1).

In the process of the cage augmentation by low-temperature strategy, the overall shifting of hydrophilicity/hydrophobicity ratio for L-FDU-12-100 is buffered because the low temperature induces hydrophilicity of block copolymers and more TMB

uptake results in the hydrophobicity. The hydrophobic segments of block copolymer micelles are generally considered to account for pore volumes of the mesoporous materials.[46] The increasing amount of TMB leads to the increase of the micelle volumes, which results in a cage diameter expansion. At the same time, the PEO segments are more relaxed at a low temperature and occupy larger corona space.[25] Consequently pore cages of L-FDU-12-100 become quite large with a very spherical shape in order to lower the surface tension (Figure 4a).

Compared with L-FDU-12-100, the circular isochromatic zones of R-FDU-12-100 are deformed with the surface curvatures decreasing along the [220] and [200] directions (Figure 4b). A similar and obvious trend is also observed for R-FDU-12-120 (Figure 4c). The inosculated cyan zone suggests that the entrances are open to the 12 neighboring cages even at a relatively small cage diameter. It has been known that the cage entrance enlargement by hydrothermal treatment is attributed to the decrease of the hydrophilicity of the PEO blocks with increased temperature.[24,37,38] From this point of view, PEO blocks can be drawn back into the micelles which increases the hydrophobic segment volume of block copolymer micelles at high hydrothermal temperature. The increased hydrophobic segment volume occupies more space in the entrance sites than in the pore cage, possibly because there is less resistance to the pore expansion in these thinnest areas of silica walls. The 3-D
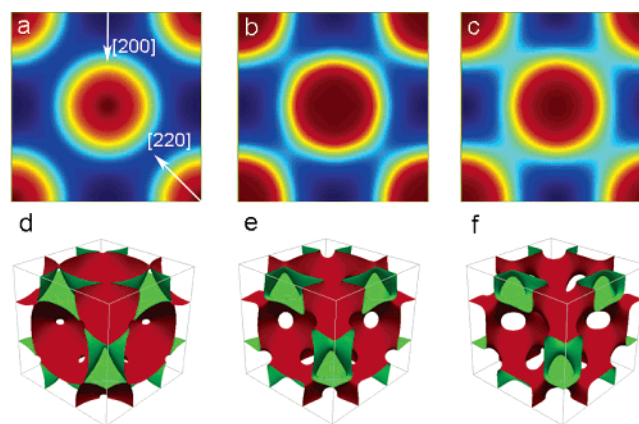

Figure 4. (a−c) 2-D sections at $z = 0$ of the electrostatic potential maps and (d−f) 3-D electrostatic potential maps of the calcined mesoporous silica: (a, d) L-FDU-12-100; (b, e), R-FDU-12-100; and (c, f), R-FDU-12-120. The contour lines of 2-D electrostatic potential maps are shown by isochromatic zone at the $z = 0$ plane. Cold hue refers to high electrostatic potential, which is closer to the silica wall herein (a−c). The arrows in panel a indicate the two specific directions perpendicular to pore surface. The red surfaces in panels d−f are toward the pores and the green surfaces toward the walls.

21472 *J. Phys. Chem. B, Vol. 110, No. 43, 2006*

Yu et al.

electrostatic potential maps obtained by electron crystallography (Figure 4d,e,f) provide even more clearly the pore expansion behaviors of FDU-12s at different synthesis and hydrothermal treatment temperatures.

Assuming the silica wall density is 2.2 g/cm^3 based on amorphous silica, the pore wall interfaces of L-FDU-12-100, R-FDU-12-100, and R-FDU-12-120 are tentatively determined from the total pore volumes. From these pore structure models given by electron crystallography and nitrogen adsorption volumes, the calculated cage diameters for the three samples are about 24.5, 18.7, and 19.3 nm, respectively, within experimental error from those calculated values of the NLDFT sphere model. However, the obtained cage entrance sizes of 2.4, 3.7, and 6.0 nm from the three FDU-12 samples only represent the entrance enlargement trend in a relative scale. An accurate determination of the 3-D pore structures of FDU-12s by HRTEM images together with nitrogen sorption requires much more on the large domain size and high phase purity, which are normally difficult to satisfy especially when samples were post-treated and bimodal[47] entrances or poorly formed pores were involved. On the other hand, the small domain structures can be studied by TEM. The 3-D reconstruction of ordered mesostructures from HRTEM images by electron crystallography, combined with PXRD, SAXS, and nitrogen sorption, can provide important information regarding the pore cage expansion and entrance enlargement.

Conclusions

A variety of FDU-12 materials synthesized at different synthesis and hydrothermal treatment temperatures are investigated by combining diffraction techniques, such as PXRD and SAXS, nitrogen sorption analysis, and electron crystallography. The space group of FDU-12s can be assigned to be *Fm$\bar{3}$m* based on the analysis of diffraction patterns and HRTEM images. The pore structures of FDU-12s are a face-centered cubic (fcc) close-packing of spherical cages, each connected to 12 nearest neigboring cages. The systematic variation in relative diffraction intensities of FDU-12s in PXRD and SAXS patterns suggested the occurrence of pore structure changes. The 3-D structure models show that the synthesis of FDU-12 at a low temperature results in not only very large pore cages but also a very spherical-like cage shape. A high-temperature hydrothermal treatment causes much more efficient enlargement of the cage entrances than that of the cages themselves, partially due to a release of expansion strains.

References and Notes

(1) Davis, M. E. *Nature* **2002**, *417*, 813.

(2) Stein, A. *Adv. Mater.* **2003**, *15*, 763.

(3) Ying, J. Y.; Mehnert, C. P.; Wong, M. S. *Angew. Chem., Int. Ed.* **1999**, *38*, 56.

(4) Kresge, C. T.; Leonowicz, M. E.; Roth, W. J.; Vartuli, J. C.; Beck, J. S. *Nature* **1992**, *359*, 710.

(5) Huo, Q. S.; Leon, R.; Petroff, P. M.; Stucky, G. D. *Science* **1995**, *268*, 1324.

(6) Bagshaw, S. A.; Prouzet, E.; Pinnavaia, T. J. *Science* **1995**, *269*, 1242.

(7) Zhao, D. Y.; Feng, J. L.; Huo, Q. S.; Melosh, N.; Fredrickson, G. H.; Chmelka, B. F.; Stucky, G. D. *Science* **1998**, *279*, 548.

(8) Zhao, D. Y.; Huo, Q. S.; Feng, J. L.; Chmelka, B. F.; Stucky, G. D. *J. Am. Chem. Soc.* **1998**, *120*, 6024.

(9) Tanev, P. T.; Pinnavaia, T. J. *Science* **1995**, *267*, 865.

(10) Yang, P. D.; Zhao, D. Y.; Margolese, D. I.; Chmelka, B. F.; Stucky, G. D. *Chem. Mater.* **1999**, *11*, 2813.

(11) Ryoo, R.; Joo, S. H.; Jun, S. *J. Phys. Chem. B* **1999**, *103*, 7743.

(12) Tian, B. Z.; Liu, X. Y.; Tu, B.; Yu, C. Z.; Fan, J.; Wang, L. M.; Xie, S. H.; Stucky, G. D.; Zhao, D. Y. *Nature Mater.* **2003**, *2*, 159.

(13) Che, S.; Liu, Z.; Ohsuna, T.; Sakamoto, K.; Terasaki, O.; Tatsumi, T. *Nature* **2004**, *429*, 281.

(14) Hatton, B.; Landskron, K.; Whitnall, W.; Perovic, D.; Ozin, G. A. *Acc. Chem. Res.* **2005**, *38*, 305.

(15) Meng, Y.; Gu, D.; Zhang, F. Q.; Shi, Y. F.; Yang, H. F.; Tu, B.; Yu, C. Z.; Zhao, D. Y. *Angew. Chem., Int. Ed.* **2005**, *44*, 7053. Wan, Y.; Yang H. F.; Zhao, D. Y. *Acc. Chem. Res.* **2006**, *39*, 423.

(16) Sakamoto, Y.; Kaneda, M.; Terasaki, O.; Zhao D. Y.; Kim, J. M.; Stucky, G. D.; Shin, H. J.; Ryoo, R. *Nature* **2000**, *408*, 449.

(17) Yu, C. Z.; Yu, Y. H.; Zhao, D. Y. *Chem. Commun.* **2000**, 575.

(18) Tattershall, C. E.; Jerome, N. P.; Budd, P. M. *J. Mater. Chem.* **2001**, *11*, 2979.

(19) Kipkemboi, P.; Fogden, A.; Alfredsson, V.; Flodstrom, K. *Langmuir* **2001**, *17*, 5398.

(20) Yu, C. Z.; Tian, B. Z.; Fan, J.; Stucky, G. D.; Zhao, D. Y. *J. Am. Chem. Soc.* **2002**, *124*, 4556.

(21) Matos, J. R.; Kruk, M.; Mercuri, L. P.; Jaroniec, M.; Zhao, L.; Kamiyama, T.; Terasaki, O.; Pinnavaia, T. J.; Liu, Y. *J. Am. Chem. Soc.* **2003**, *125*, 821.

(22) Fan, J.; Yu, C. Z.; Gao, T.; Lei, J.; Tian, B. Z.; Wang, L. M.; Luo, Q.; Tu, B.; Zhou, W. Z.; Zhao, D. Y. *Angew. Chem., Int. Ed.* **2003**, *42*, 3146.

(23) Kleitz, F.; Liu, D. N.; Anilkumar, G. M.; Park, I. S.; Solovyov, L. A.; Shmakov, A. N.; Ryoo, R. *J. Phys. Chem. B* **2003**, *107*, 14296.

(24) Kim, T.-W.; Ryoo, R.; Kruk, M.; Gierszal, K. P.; Jaroniec, M.; Kamiya, S.; Terasaki, O. *J. Phys. Chem. B* **2004**, *108*, 11480.

(25) Fan, J.; Yu, C. Z.; Lei, J.; Zhang, Q.; Li, T. C.; Tu, B.; Zhou, W. Z.; Zhao, D. Y. *J. Am. Chem. Soc.* **2005**, *127*, 10794.

(26) Kruk, M.; Celer, E. B.; Matos, J. R.; Pikus, S.; Jaroniec, M. *J. Phys. Chem. B* **2005**, *109*, 3838.

(27) Shui, W. Q.; Fan, J.; Yang, P. Y.; Liu, C. L.; Zhai, J. J.; Lei, J.; Yan, Y.; Zhao, D. Y.; Chen, X. *Anal. Chem.* **2006**, *78*, 4811.

(28) Zhou, W. Z.; Hunter, H. M. A.; Wright, P. A.; Ge, Q. F.; Thomas, J. M. *J. Phys. Chem. B* **1998**, *102*, 6933.

(29) Kaneda, M.; Tsubakiyama, T.; Carlsson, A.; Sakamoto, Y.; Ohsuna, T.; Terasaki, O.; Joo, S. H.; Ryoo, R. *J. Phys. Chem. B* **2002**, *106*, 1256.

(30) Sakamoto, Y.; Diaz, I.; Terasaki, O.; Zhao, D. Y.; Perez-Pariente, J.; Kim, J. M.; Stucky, G. D. *J. Phys. Chem. B* **2002**, *106*, 3118.

(31) Sakamoto, Y.; Kim, T. W.; Ryoo, R.; Terasaki, O. *Angew. Chem., Int. Ed.* **2004**, *43*, 5231.

(32) Garcia-Bennett, A. E.; Terasaki, O.; Che, S.; Tatsumi, T. *Chem. Mater.* **2004**, *16*, 813.

(33) Garcia-Bennett, A. E.; Miyasaka, K.; Terasaki, O.; Che, S. *Chem. Mater.* **2004**, *16*, 3597.

(34) Gao, C. B.; Sakamoto, Y.; Sakamoto, K.; Terasaki, O.; Che, S. *Angew. Chem., Int. Ed.* **2006**, *45*, 1.

(35) Ravikovitch, P. I.; Neimark, A. V. *Langmuir* **2002**, *18*, 1550.

(36) Ustinov, E. A.; Do, D. D.; Jaroniec, M. *J. Chem. Theory Comput.* **2005**, *1*, 653.

(37) Galarneau, A.; Cambon, H.; Di Renzo, F.; Fajula, F. *Langmuir* **2001**, *17*, 8328.

(38) Van Der Voort, P.; Benjelloun, M.; Vansant, E. F. *J. Phys. Chem. B* **2002**, *106*, 9027.

(39) Booth, C.; Attwood, D. *Macromol. Rapid Commun.* **2000**, *21*, 501.

(40) Hovmöller, S. *Ultramicroscopy* **1992**, *41*, 121.

(41) Oleynikov, P.; Zou, X. D.; Hovmöller, S. http://www.analitex.com/Index.html, 2006.

(42) Zou, X. D.; Mo, Z. M.; Hovmöller, S.; Li, X. Z.; Kuo, K. H. *Acta Crystallogr.* **2003**, *A59*, 526.

(43) Imperor-Clerc, M.; Davidson, P.; Davidson, A. *J. Am. Chem. Soc.* **2000**, *122*, 11925.

(44) Solovyov, L. A.; Kirik, S. D.; Shmakov A. N.; Romannikov, V. N. *Microporous Mesoporous Mater.* **2001**, *44−45*, 17.

(45) Solovyov, L. A.; Kim, T.-W.; Kleitz, F.; Terasaki, O.; Ryoo, R. *Chem. Mater.* **2004**, *16*, 2274.

(46) Yu, C. Z.; Fan, J.; Tian, B. Z.; Stucky, G. D.; Zhao, D. Y. *J. Phys. Chem. B* **2003**, *107*, 13368.

(47) El-Safty, S. A.; Hanaoka, T.; Mizukami, F. *Chem. Mater.* **2005**, *17*, 3137.